ADVANCED MATERIALS

Supporting Information

for *Adv. Mater.,* DOI: 10.1002/adma.202109304

Optimally-Tailored Spinodal Architected Materials for Multiscale Design and Manufacturing

*Fernando V. Senhora, Emily D. Sanders, and Glaucio H. Paulino**

Supporting Information

Optimally-tailored spinodal architected materials for multiscale design and manufacturing

Fernando V. Senhora, Emily D. Sanders, Glaucio H. Paulino*

Contents

S1 Spinodal architected materials **3**

S1.1 Definition of spinodal architected materials with tuned anisotropy . . . 3

S1.2 Mechanical properties of candidate spinodal architected materials . . . 5

S2 Spinodal topology optimization **5**

S2.1 Problem setting and optimization formulation . . . 6

S2.2 Gradient-based solution scheme . . . 9

S2.3 Sensitivity analysis . . . 9

S3 Spatially-varying stiffness elasticity tensor **11**

S3.1 Spatially-varying porosity . . . 11

S3.2 Spatially-varying orientation . . . 12

S4 Additional details of the design examples **14**

S4.1 Topology optimization algorithmic parameters and computational resources . . . 14

S4.2 Standard topology optimization solutions . . . 15

S4.3 Spinodal density variation . . . 15

S5 Additive Manufacturing **16**

S5.1 Processing optimized spinodal-embedded parts for additive manufacturing . . . 16

S5.2 Spinodal parameters for manufacturing . . . 19

S1 Spinodal architected materials

Spinodal decomposition [1] occurs when two phases spontaneously separate without nucleation of the system. Systems that allow spinodal-like phase separation exist in a local maximum energy state, and therefore, random fluctuations in the concentration of the two-phases reduce the free energy of the system causing the spontaneous separation. The spinodal separation of phases can be modeled by the Cahn–Hilliard equation [2, 3],

$$\frac{\partial c}{\partial t} = D\nabla^2 \left(c^3 - c - \omega\nabla^2 c\right), \tag{S1}$$

where c is the concentration of the two phases, D is a diffusion coefficient, and ω is related to the transition region between phases.

S1.1 Definition of spinodal architected materials with tuned anisotropy

Equation S1 is computationally expensive to solve and provides limited control over the spinodal decomposition phase separation; however, the phase field characterizing a spinodal phase decomposition of a homogeneous solution can be approximated by a Gaussian random field of the form,

$$\phi\left(\mathbf{x}\right) = \sqrt{\frac{2}{N}} \sum_{i=1}^{N} \cos\left(\kappa \mathbf{n}_i \cdot \mathbf{x} + \mu_i\right), \tag{S2}$$

as the number of waves, N, goes to infinity [4, 5]. Equation S2 is a more convenient representation of spinodal phase decomposition than Equation S1 and provides freedom to manipulate the form of the assciated phase field. Each wave in Equation S2 has the same amplitude and wavelength controlled by N and κ, respectively. The phase shift of wave i, $\mu_i \in \mathcal{U}\left[0, 2\pi\right)$, is randomly sampled from a uniform distribution. When the number of wave vectors is large, $\phi\left(\mathbf{x}\right)$ is statistically homogeneous. Furthermore, when the wave vectors, $\mathbf{n}_i,\ i = 1, \ldots, N$, are randomly sampled from the unit sphere, i.e., $\mathbf{n}_i \in \mathcal{U}\left[\mathbb{S}^2\right]\ \forall i$, $\phi\left(\mathbf{x}\right)$ is statistically isotropic; however, when the space of wave vectors is restricted, $\phi\left(\mathbf{x}\right)$ becomes statistically anisotropic.

The phase field, $\phi\left(\mathbf{x}\right)$, has been interpreted as a mechanical (spinodal) architected material characterized by the level set function,

$$\chi\left(\mathbf{x}\right) = \begin{cases} 1 & \text{if } \phi\left(\mathbf{x}\right) \leq \phi_{\text{cut}}\left(\rho\right) \\ 0 & \text{otherwise,} \end{cases} \tag{S3}$$

such that one phase of the spinodal phase decomposition is interpreted as solid material and the other as

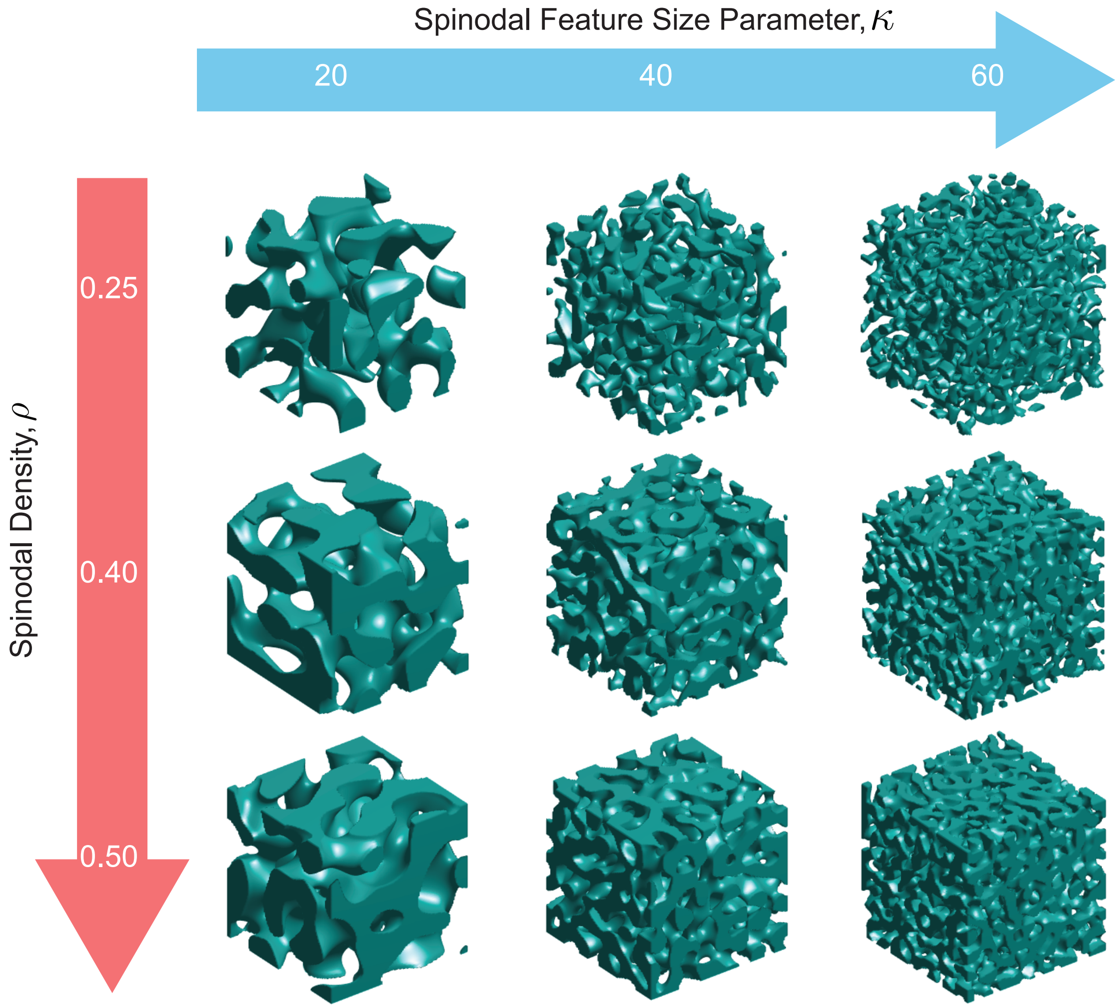

Figure S1: Effect of spinodal feature size parameter, κ, and spinodal density, ρ, on the spinodal microstructure of the isotropic spinodal class. By varying κ we can directly and arbitrarily tune the microstructure length scale, and by varying ρ we can locally control the density of the architected material. Notice that for $\rho = 0.25$ the microstructure starts to become disconnected.

void. The level set cutoff is defined as $\phi_{\text{cut}}(\rho) = \sqrt{2}\text{erf}^{-1}(2\rho - 1)$, where ρ controls the density of solid material [5]. In this context, κ in Equation S2 is interpreted as the spinodal feature size parameter that controls the length scale of the spinodal features. The influence of the spinodal feature size parameter, κ, and the spinodal density, ρ, are displayed in **Figure S1** for an isotropic spinodal architected material.

The associated spinodal architected materials considered here inherit the statistical properties of the phase field function, $\phi(\mathbf{x})$, and thus, by restricting the space of wave vectors, anisotropic mechanical properties of the spinodal architected material can be tuned [6, 7]. To define the four spinodal architected materials considered here, the space of wave vectors is restricted such that,

$$\mathbf{n}_i \in \mathcal{U}\left[\{\mathbf{m} \in \mathbb{S}^2 : (|\mathbf{m} \cdot \mathbf{e}_1| > \cos\theta_1) \oplus (|\mathbf{m} \cdot \mathbf{e}_2| > \cos\theta_2) \oplus (|\mathbf{m} \cdot \mathbf{e}_3| > \cos\theta_3)\}\right], \tag{S4}$$

where $\mathbf{e}_1$, $\mathbf{e}_2$, and $\mathbf{e}_3$ form the Cartesian basis of $\mathbb{R}^3$ and $\theta_1, \theta_2, \theta_3 \in [0, \pi/2]$ are cone angles [7]. The specific choice of isotropic, cubic, lamellar, and columnar spinodal architected materials used as candidates in topology optimization are defined by the following cone angles (refer to Figure 3 in the main text): 1) for isotropic, there is no restriction; 2) for cubic, $\theta_1 = \theta_2 = \theta_3 = 30°$, 3) for lamellar, $\theta_1 = 30°$, $\theta_2 = \theta_3 = 0°$; and 4) for columnar, $\theta_1 = \theta_2 = 30°$, $\theta_3 = 0°$. Note that to avoid sparse connections between the lamella of the lamellar spinodal microarchitectures, we restrict only 85% of the wave vectors to the cones defined above, and allow 15% to fall anywhere on the unit sphere. Although the cone angles for each case are fixed during the optimization, the four selected spinodal architected materials cover a significant portion of the design space since the topology optimization formulation can vary their porosity and orientation in 3D space.

S1.2 Mechanical properties of candidate spinodal architected materials

Mechanical properties of the spinodal architected materials are obtained using an educational Matlab implementation [8] of computational homogenization [9] that outputs the homogenized stiffness elasticity tensor (in matrix notation) for a representative volume element of a given microstructural-material. The solid (base) material used has a Young's modulus and Poisson's ratio of 1 and 0.3, respectively. The computational homogenization is performed considering the spinodal phase field (with $\kappa = 100$) and associated level set function defined on a unit cube, which is discretized into a $100 \times 100 \times 100$ hexahedral (hex) finite element mesh. Due to statistical homogeneity, any region of the spinodal field behaves statistically the same as any other region [6]. As a result, it has been shown for isotropic spinodal architected materials that computational homogenization leads to almost identical mechanical properties for periodic and non-periodic realizations when N is large [5]. For practical reasons, the number of wave vectors used to approximate the spinodal phase field is limited here to a finite value, $N = 1000$, which limits the statistical homogeneity of the phase field. Thus, the homogenized mechanical properties for each class of spinodal architected materials are taken as the average of those obtained from 15 realizations of the phase field. The average and maximum relative standard deviation of these samples is 0.04 and 0.15, respectively. The low standard deviation shows the robustness of the spinodal mechanical properties and provides evidence that, given sufficient separation of scale, the spinodal mechanical properties are independent of the realization and are not negatively affected by the randomness of the spinodal features.

S2 Spinodal topology optimization

The classical homogenization-based topology optimization formulation proposed by Bendsoe and Kikuchi in 1988 [10] is integrated with a recent multi-microstructural-material topology optimization formulation [11], to achieve a volume-constrained compliance minimization formulation that simultaneously determines the placement, orientation, and porosity of several classes of spinodal architected materials (spinodal topology optimization). The approach is summarized in **Figure S2**.

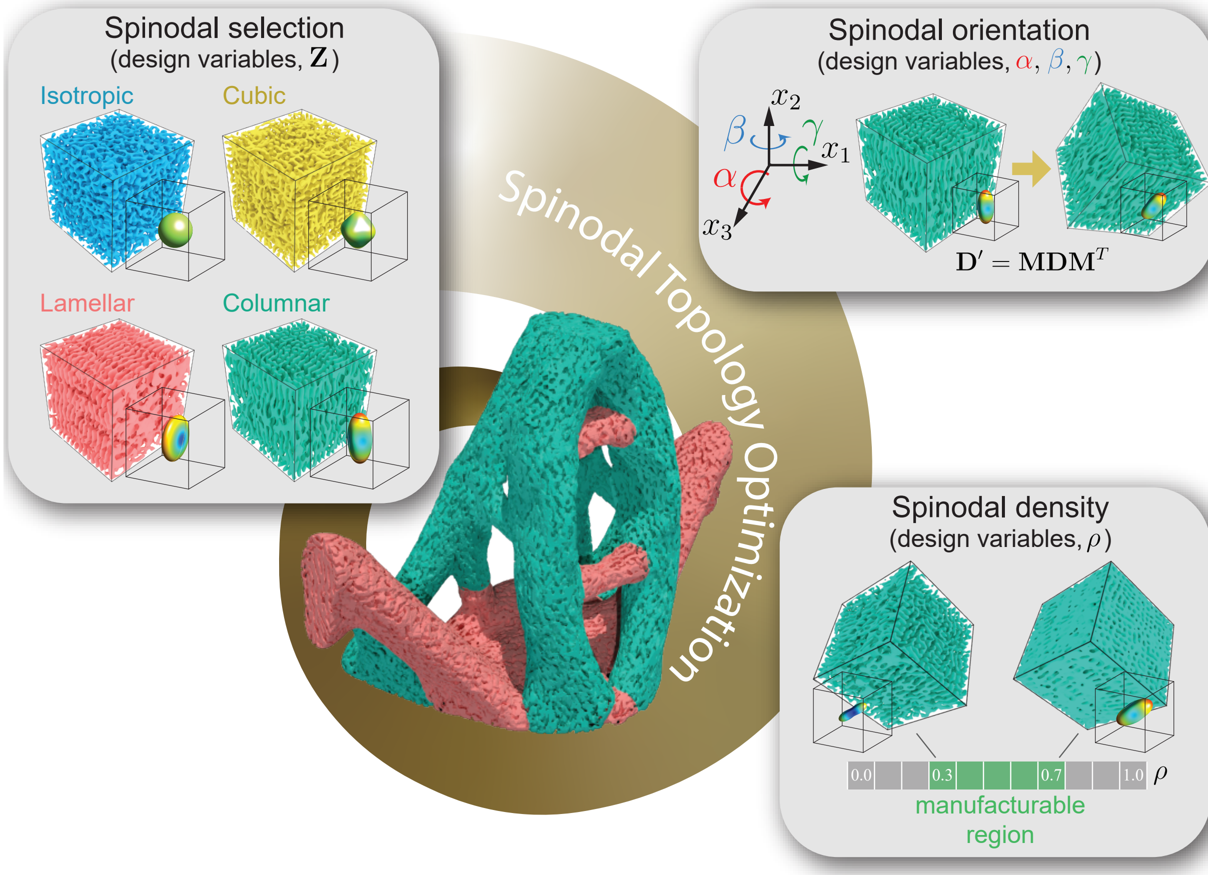

Figure S2: Overview of spinodal topology optimization.

S2.1 Problem setting and optimization formulation

The spinodal topology optimization problem is stated as

$$\begin{aligned}
\min_{\mathbf{Z},\boldsymbol{\rho},\boldsymbol{\alpha},\boldsymbol{\beta},\boldsymbol{\gamma}} \quad & f = \mathbf{F}^T\mathbf{U}\left(\mathbf{Z},\boldsymbol{\rho},\boldsymbol{\alpha},\boldsymbol{\beta},\boldsymbol{\gamma}\right) \\
\text{s.t.} \quad & g_j = \frac{\sum_{i\in\mathcal{G}_j}\sum_{\ell\in\mathcal{E}_j} A_\ell v_{\ell i}}{\sum_{\ell\in\mathcal{E}_j} A_\ell} - \overline{v}_j \leq 0, \qquad j = 1,\ldots,K \\
\text{with} \quad & \mathbf{K}\left(\mathbf{Z},\boldsymbol{\rho},\boldsymbol{\alpha},\boldsymbol{\beta},\boldsymbol{\gamma}\right)\mathbf{U}\left(\mathbf{Z},\boldsymbol{\rho},\boldsymbol{\alpha},\boldsymbol{\beta},\boldsymbol{\gamma}\right) = \mathbf{F}.
\end{aligned} \tag{S5}$$

In Equation S5, the objective function, f, is structural compliance and the constraint function, g_j, enforces volume fraction limit, $\overline{v}_j$, for constraints $j = 1,\ldots,K$. Five sets of design variables are defined at the centroids of N^e elements, $\{\Omega_\ell\}_{\ell=1}^{N^e}$, used to discretize the design domain, Ω. The spinodal selection design variable field, $\mathbf{Z} = \{z_{\ell 1}, \ldots, z_{\ell m}\}_{\ell=1}^{N^e}$, controls the presence or absence of each of the $i = 1, \ldots, m$ candidate spinodal architected materials at each of the $\ell = 1, \ldots, N^e$ elements, where component $z_{\ell i} \in [0, 1]$; the spinodal density design variable field, $\boldsymbol{\rho} = \{\rho_\ell\}_{\ell=1}^{N^e}$, controls the local solid volume fraction of the spinodal architected material at each of the $\ell = 1, \ldots, N^e$ elements, where component $\rho_\ell \in [\underline{\rho}, \overline{\rho}]$ and $0 \leq \underline{\rho}, \overline{\rho} \leq 1$ are selected based on manufacturing requirements; and the spinodal orientation design variable fields, $\boldsymbol{\alpha} = \{\alpha_\ell\}_{\ell=1}^{N^e}$, $\boldsymbol{\beta} = \{\beta_\ell\}_{\ell=1}^{N^e}$, and $\boldsymbol{\gamma} = \{\gamma_\ell\}_{\ell=1}^{N^e}$, control the rotation of the spinodal architected materials at each of the $\ell = 1, \ldots, N^e$ elements about the x_3, x_2, and x_1 axes of a reference frame, respectively, where components $\alpha_\ell, \beta_\ell, \gamma_\ell \in [-\pi, \pi]$. Note that the orientation design variables, $\boldsymbol{\alpha}$, $\boldsymbol{\beta}$, and $\boldsymbol{\gamma}$, are defined using modular arithmetic with a period of 2π. As a result, the domain of these design variables is topologically equivalent to a circle, which allows the angles to traverse directly from π to $-\pi$.

To enforce well-posedness of the problem and a minimum length scale on the design, the elemental spinodal field, $\mathbf{Y} = \{y_{\ell 1}, \ldots, y_{\ell m}\}_{\ell=1}^{N^e}$, is obtained as $\mathbf{y}_i = \mathbf{P}\mathbf{z}_i$, where $\mathbf{y}_i$ and $\mathbf{z}_i$ are the i^{th} column of $\mathbf{Y}$ and $\mathbf{Z}$, respectively, and $\mathbf{P}$ is a regularization map (density filter [12, 13]) with coefficients

$$P_{ij} = \frac{h_{ij} A_j}{\sum_{k=1}^{N^e} h_{ik} A_k}, \quad h_{ij} = \max\left[0, (R - ||\mathbf{x}_i - \mathbf{x}_j||_2)^q\right]. \tag{S6}$$

In Equation S6, $||\mathbf{x}_i - \mathbf{x}_j||_2$ is the Euclidean norm between the centroids of elements i and j, R is the filter radius, and q defines the order of the filter [14] (e.g., linear filter when $q = 1$). Additionally, to penalize intermediate values in spinodal architected material selection, a SIMP interpolation [15, 16] is coupled with a Heaviside projection [17, 18], $\tilde{\mathbf{Y}} = \{\tilde{y}_{\ell 1}, \ldots, \tilde{y}_{\ell m}\}_{\ell=1}^{N^e}$, of the elemental spinodal field to obtain a penalized elemental spinodal field, $\mathbf{W} = \{w_{\ell 1}, \ldots, w_{\ell m}\}_{\ell=1}^{N^e}$, where component $w_{\ell i} = \tilde{y}_{\ell i}^p$ with $p > 1$. Components of the projected field are obtained as

$$\tilde{y}_{\ell i} = \frac{\tanh(\xi\eta) + \tanh(\xi(y_{\ell i} - \eta))}{\tanh(\xi\eta) + \tanh(\xi(1 - \eta))}, \; 1 \geq \eta \geq 0, \; \xi \geq 0. \tag{S7}$$

in which η is the value of the threshold for the Heaviside function approximation and ξ controls the sharpness of such approximation.

The formulation in Equation S5 also includes $j = 1, \ldots, K$ volume constraints that control any subset of the candidate materials in any subregion of the domain. As such, $\mathcal{G}_j$ and $\mathcal{E}_j$ represent the set of material and element indices associated with constraint j, respectively [19, 20, 21, 11]. Furthermore, A_ℓ represents the volume of element ℓ; $\mathbf{V} = \{v_{\ell 1}, \ldots, v_{\ell m}\}_{\ell=1}^{N^e}$ is the material volume fraction for each of the $i = 1, \ldots, m$ candidate spinodal architected materials at each of the $\ell = 1, \ldots, N^e$ elements, where component $v_{\ell i} = \tilde{y}_{\ell i}\rho_\ell$; and $\overline{v}_j$ is the volume fraction limit for constraint j. When the subscript, j, is omitted, it is understood that there is only one volume constraint.

The same discretization used for the optimization problem is also used to solve for the displacement field, $\mathbf{U}$, via the discretized state equations of static elasticity, $\mathbf{K}(\mathbf{Z}, \boldsymbol{\rho}, \boldsymbol{\alpha}, \boldsymbol{\beta}, \boldsymbol{\gamma})\,\mathbf{U}(\mathbf{Z}, \boldsymbol{\rho}, \boldsymbol{\alpha}, \boldsymbol{\beta}, \boldsymbol{\gamma}) = \mathbf{F}$. In the state equations, the stiffness matrix, $\mathbf{K} = \mathbb{A}_{\ell=1}^{N^e}\mathbf{k}_\ell$, is assembled from the element stiffness matrices, $\mathbf{F}_i = \int_{\tilde{\Gamma}_N} \mathbf{t} \cdot \mathbf{N}_i ds$ is the vector of design-independent nodal loads, $\mathbf{t}$ is the traction applied on the portion, $\tilde{\Gamma}_N$, of the domain boundary, and $\mathbf{N}$ is the vector of interpolation (shape) functions used to interpolate quantities between the mesh nodal points.

The mechanical properties of the spatially-varying spinodal architected materials are embedded in the element stiffness matrices,

$$(\mathbf{k}_\ell)_{jk} = \int_{\Omega_\ell} \mathbf{B}_j^T \mathbf{D}_\ell\left(\mathbf{w}'_\ell, \rho_\ell, \alpha_\ell, \beta_\ell, \gamma_\ell\right)\mathbf{B}_k d\mathbf{x}, \tag{S8}$$

where $\mathbf{B}$ is the strain-displacement matrix of shape function derivatives, $\mathbf{w}'_\ell$ is the ℓ^{th} row of $\mathbf{W}$, and $\mathbf{D}_\ell$ is the stiffness elasticity tensor (in matrix notation) in element ℓ. The stiffness elasticity matrix is obtained via a multi-material interpolation function,

$$\mathbf{D}_\ell = \sum_{i=1}^{m} w_{\ell i} \prod_{\substack{j=1 \\ j\neq i}}^{m} \left(1 - \tilde{\gamma} w_{\ell j}\right) \mathbf{M}\left(\alpha_\ell, \beta_\ell, \gamma_\ell\right) \mathbf{D}_i^H\left(\rho_\ell\right) \mathbf{M}^T\left(\alpha_\ell, \beta_\ell, \gamma_\ell\right), \quad \ell = 1, \ldots, N^e, \tag{S9}$$

that penalizes mixing between the candidate spinodal architected materials, where $0 < \tilde{\gamma} < 1$ controls the amount of allowable mixing [22, 21]; $\mathbf{M}$ is a matrix that performs the fourth-order tensor transformations in matrix notation (see Section S3.2); and $\mathbf{D}_i^H(\rho_\ell)$ is the homogenized stiffness elasticity matrix of spinodal architected material i in element ℓ in the reference frame. Each component of the homogenized stiffness elasticity tensor is approximated as a function of spinodal density (pre-optimization) as $\left(\mathbf{D}_i^H\right)_{jk}(\rho_\ell) = \left(\mathcal{F}_i\right)_{jk}(\rho_\ell)$, according to fitting function, $\mathcal{F}_i$, for spinodal architected material i (see Section S3.1).

It is noted that the orientation design variables make the optimization problem significantly more complex and prone to undesirable local optima. One way to mitigate this issue is to define a set of orientation design variables for each spinodal architected material at each point in the domain rather than a single set of orientation design variables. Here, the extra computational cost associated with this approach was deemed not worth the marginal gain in design freedom; however, most of these extra computations are highly parallelizable and a parallel GPU implementation could greatly increase the computational efficiency in considering this more comprehensive set of design variables.

S2.2 Gradient-based solution scheme

The optimization problem in Equation S5 is solved using an iterative optimization algorithm based on gradient descent and the augmented Lagrangian (AL) method [23, 24]. In the AL method, we solve a series of unconstrained, surrogate problems where the AL function to be minimized in each outer iteration, t, is the sum of the original objective function, f, plus an adaptive penalty term that is a function of the original constraints, $g_j, j = 1, \ldots, K$. The AL function is stated as

$$AL(\mathbf{x})^{(t)} = f(\mathbf{x}) + \sum_{j=1}^{K} \left[\lambda_j^{(t)} \max(g_j(\mathbf{x}), -\lambda_j^{(t)}/\mu^{(t)}) + \frac{\mu^{(t)}}{2} \max(g_j(\mathbf{x}), -\lambda_j^{(t)}/\mu^{(t)})^2 \right], \tag{S10}$$

where $\lambda_j^{(t)}, j = 1, \ldots, K$ and $\mu^{(t)}$ are penalization parameters that are updated every five inner optimization iterations as

$$\lambda_j^{(t+1)} = \lambda_j^{(t)} + \mu \max(g_j(\mathbf{x}), -\lambda_j^{(t)}/\mu^{(t)}) \ \text{ and } \ \mu^{(t+1)} = 1.25\mu^{(t)}. \tag{S11}$$

For well-posed problems like that in Equation S5, the AL method is guaranteed to converge to a feasible solution, given enough iterations.

At each inner optimization iteration, k, we update the design variables according to

$$\mathbf{x}^{(k+1)} = \max \left[\min \left(\mathbf{x}^{(k)} - \tau^{(k)} \frac{\partial (AL)}{\partial \mathbf{x}}, \mathbf{x}^{(k)} + mv \right), \mathbf{x}^{(k)} - mv \right], \tag{S12}$$

where $\mathbf{x}$ is a vector holding all design variables defined in Equation S5, mv is a move limit, and τ is a step size, which is updated at each inner iteration such that $\tau^{(k+1)} = \max(0.99\tau^{(k)},\ 0.01)$, with $\tau^{(0)} = 1$.

We consider a staggered update during the first 150 inner optimization iterations, in which, every 25 inner iterations, we run 30 additional sub-iterations that only update the orientation design variables. These sub-iterations are meant to promote spinodal microarchitecture alignment with the principal stress directions of the macrostructure and guide the optimization to a better local minimum.

S2.3 Sensitivity analysis

To update the design variables as described, the sensitivities of the objective function, f, and constraint functions, $g_j, j = 1, \ldots, K$, with respect to each set of design variables are needed. Such derivatives of f are computed as

$$\frac{\partial f}{\partial \mathbf{z}_i} = \frac{\partial \mathbf{y}_i}{\partial \mathbf{z}_i} \frac{\partial \tilde{\mathbf{y}}_i}{\partial \mathbf{y}_i} \frac{\partial \mathbf{w}_i}{\partial \tilde{\mathbf{y}}_i} \frac{\partial f}{\partial \mathbf{w}_i}, \text{ where } \frac{\partial f}{\partial w_{\ell i}} = -\mathbf{U}^T \frac{\partial \mathbf{K}}{\partial w_{\ell i}} \mathbf{U}, \tag{S13}$$

$$\frac{\partial f}{\partial \rho_\ell} = -\mathbf{U}^T \frac{\partial \mathbf{K}}{\partial \rho_\ell} \mathbf{U}, \tag{S14}$$

$$\frac{\partial f}{\partial \alpha_\ell} = -\mathbf{U}^T \frac{\partial \mathbf{K}}{\partial \alpha_\ell} \mathbf{U}, \; \frac{\partial f}{\partial \beta_\ell} = -\mathbf{U}^T \frac{\partial \mathbf{K}}{\partial \beta_\ell} \mathbf{U}, \text{ and } \frac{\partial f}{\partial \gamma_\ell} = -\mathbf{U}^T \frac{\partial \mathbf{K}}{\partial \gamma_\ell} \mathbf{U}. \tag{S15}$$

In Equation S13, the first three components are $\partial \mathbf{y}_i / \partial \mathbf{z}_i = \mathbf{P}^T$,

$$\frac{\partial \tilde{y}_{kj}}{\partial y_{\ell i}} = \begin{cases} \dfrac{\xi(1 - \tanh^2(\xi(y_{\ell i} - \eta)))}{\tanh(\xi\eta) + \tanh(\xi(1-\eta))}, & \text{if } \ell = k \text{ and } j = i \\ 0, & \text{otherwise,} \end{cases} \quad \text{and} \quad \frac{\partial w_{kj}}{\partial \tilde{y}_{\ell i}} = \begin{cases} p\tilde{y}_{\ell i}^{p-1}, & \text{if } \ell = k \text{ and } j = i \\ 0, & \text{otherwise.} \end{cases} \tag{S16}$$

The remaining derivatives in Equation S13 to Equation S15 all have the same form and require derivatives of the stiffness matrix, which can be computed at the element level. From Equation S8, it is clear that these derivatives rely on the derivatives of the stiffness elasticity matrix, which are computed as

$$\frac{\partial \mathbf{D}_k}{\partial w_{\ell i}} = \begin{cases} \displaystyle\prod_{\substack{j=1 \\ j \neq i}}^{m} (1 - \gamma w_{\ell j}) \, [\mathbf{D}_{\ell i}^H]' - \sum_{\substack{p=1 \\ p \neq i}}^{m} \gamma w_{\ell p} \prod_{\substack{r=1 \\ r \neq p \\ r \neq i}}^{m} (1 - \gamma w_{\ell r}) \, [\mathbf{D}_{\ell p}^H]', & \text{if } \ell = k \\ 0, & \text{otherwise} \end{cases} \tag{S17}$$

and

$$\frac{\partial \mathbf{D}_k}{\partial \rho_\ell} = \sum_{i=1}^{m} w_{\ell i} \prod_{\substack{j=1 \\ j \neq i}}^{m} (1 - \tilde{\gamma} w_{\ell j}) \, \frac{[\mathbf{D}_{ki}^H]'}{\partial \rho_\ell}, \tag{S18}$$

where $\partial \mathbf{D}_k / \partial \alpha_\ell$, $\partial \mathbf{D}_k / \partial \alpha_\ell$, and $\partial \mathbf{D}_k / \partial \alpha_\ell$ have the same form as Equation S18. In Equation S17 and Equation S18, the notation is simplified by denoting $[\mathbf{D}_{\ell i}^H]' = \mathbf{M}_\ell \mathbf{D}_i^H(\rho_\ell)\, \mathbf{M}_\ell^T$, where the simplified notation, $\mathbf{M}_\ell$, indicates the dependence of $\mathbf{M}$ on $\alpha_\ell, \beta_\ell, \gamma_\ell$. Then,

$$\frac{\partial [\mathbf{D}_{ki}^H]'}{\partial \rho_\ell} = \mathbf{M}_k \frac{\partial \mathbf{D}_i^H(\rho_k)}{\partial \rho_\ell} \mathbf{M}_k^T, \text{ where component } \frac{\left(\partial \mathbf{D}_i^H\right)_{pq}}{\partial \rho_\ell} = \begin{cases} \dfrac{\partial \left(\mathcal{F}_i\right)_{pq}}{\partial \rho_\ell}, & \text{if } \ell = k \\ 0, & \text{otherwise.} \end{cases} \tag{S19}$$

Similar derivatives with respect to the orientation variables take the form

$$\frac{\partial [\mathbf{D}_{ki}^H]'}{\partial \alpha_\ell} = \begin{cases} \dfrac{\partial \mathbf{M}_k}{\partial \alpha_\ell} \mathbf{D}_i^H \mathbf{M}_k^T + \mathbf{M}_k \mathbf{D}_i^H \dfrac{\partial \mathbf{M}_k^T}{\partial \alpha_\ell}, & \text{if } \ell = k \\ 0, & \text{otherwise,} \end{cases} \tag{S20}$$

with $\partial[\mathbf{D}_{ki}^{H}]'/\partial\beta_\ell$ and $\partial[\mathbf{D}_{ki}^{H}]'/\partial\gamma_\ell$ of similar form.

The derivative of the constraint functions with respect to each set of design variables are computed as

$$\frac{\partial g_j}{\partial \mathbf{z}_i} = \frac{\partial \mathbf{y}_i}{\partial \mathbf{z}_i}\frac{\partial \tilde{\mathbf{y}}_i}{\partial \mathbf{y}_i}\frac{\partial \mathbf{v}_i}{\partial \tilde{\mathbf{y}}_i}\frac{\partial g_j}{\partial \mathbf{v}_i} \text{ and } \frac{\partial g_j}{\partial \boldsymbol{\rho}} = \frac{\partial \mathbf{v}_i}{\partial \boldsymbol{\rho}}\frac{\partial g_j}{\partial \mathbf{v}_i}. \tag{S21}$$

In Equation S21, the components that have not been defined previously are

$$\frac{\partial v_{\ell i}}{\partial \tilde{y}_{jk}} = \begin{cases} \rho_\ell, & \text{if } \ell = k \text{ and } j = i \\ 0, & \text{otherwise,} \end{cases} \tag{S22}$$

$$\frac{\partial v_{\ell i}}{\partial \rho_k} = \begin{cases} \tilde{y}_{\ell i}, & \text{if } \ell = k \\ 0, & \text{otherwise, and} \end{cases} \tag{S23}$$

$$\frac{\partial g_j}{\partial v_{\ell i}} = \frac{A_\ell}{\sum_{\ell \in \mathcal{E}_j} A_\ell}. \tag{S24}$$

S3 Spatially-varying stiffness elasticity tensor

The topology optimization formulation proposed in Equation S5 allows the candidate spinodal microarchitectures to vary in porosity and orientation. Here, we describe how the homogenized stiffness elasticity tensor associated with spinodal microarchitecture i in element ℓ is computed during topology optimization according to the values of design variables, ρ_ℓ, α_ℓ, β_ℓ, and γ_ℓ. Numerical experiment indicates that positive definiteness of the homogenized stiffness elasticity tensor is preserved after these operations.

S3.1 Spatially-varying porosity

The homogenized stiffness elasticity matrix for spinodal architected material i in element ℓ, $\mathbf{D}_i^H(\rho_\ell)$, is pre-computed in the reference (unprime) frame for $\rho = 0.3, 0.4, 0.5, 0.6, 0.7$. Each component is subsequently fitted with a fourth order polynomial of the form

$$(\mathcal{F}_i)_{jk} = \sum_{s=0}^{4} (c_s)_{jk}\, \rho^s, \tag{S25}$$

where $c_s, s = 0, \ldots, 4$ are coefficients that may differ for each jk component of $\mathbf{D}_i^H(\rho_\ell)$. The data points (mean values of 15 spinodal realizations) and fitted curves are shown in Figure 3 of the main text for each non-zero component of the stiffness elasticity matrix associated with each spinodal architected material considered here.

S3.2 Spatially-varying orientation

The rotation matrix, $\mathbf{M}(\alpha_\ell, \beta_\ell, \gamma_\ell)$, used to orient the homogenized stiffness elasticity matrix is constructed from tensor transformation laws. In the following, the material and element indices, i and ℓ, as well as the superscript, H, indicating homogenized properties, are dropped for simplicity of notation.

Material properties of the spinodal architected materials are described by the fourth order stiffness elasticity tensor $C_{ijk\ell}$ that relates Cauchy stress, σ_{ij}, to linearized strain, $\varepsilon_{k\ell}$, via Hooke's law, $\sigma_{ij} = C_{ijk\ell}\varepsilon_{k\ell}, \ i,j,k,\ell = 1,2,3$. Tensor transformation laws can be used to determine the stiffness elasticity tensor, $C'_{ijk\ell}$, in any rotated (prime) frame relative to the reference (unprime) frame.

Let $\mathbf{R}$ be a direction cosine matrix that transforms vectors from the reference to the rotated frame via a general rotation, i.e., $x'_i = R_{ij}x_j$. The direction cosine matrix can be constructed as the product of three proper orthogonal matrices,

$$\mathbf{R}_1(\gamma) = \begin{bmatrix} 1 & 0 & 0 \\ 0 & c_\gamma & -s_\gamma \\ 0 & s_\gamma & c_\gamma \end{bmatrix}, \ \mathbf{R}_2(\beta) = \begin{bmatrix} c_\beta & 0 & s_\beta \\ 0 & 1 & 0 \\ -s_\beta & 0 & c_\beta \end{bmatrix}, \ \mathbf{R}_3(\alpha) = \begin{bmatrix} c_\alpha & -s_\alpha & 0 \\ s_\alpha & c_\alpha & 0 \\ 0 & 0 & 1 \end{bmatrix}, \tag{S26}$$

such that

$$\mathbf{R} = \mathbf{R}_1^T(\gamma)\,\mathbf{R}_2(\beta)\,\mathbf{R}_3^T(\alpha) = \begin{bmatrix} c_\beta c_\alpha & c_\beta s_\alpha & s_\beta \\ -s_\gamma s_\beta c_\alpha - c_\gamma s_\alpha & -s_\alpha s_\gamma s_\beta + c_\gamma c_\alpha & s_\gamma c_\beta \\ -c_\alpha c_\gamma s_\beta + s_\alpha s_\gamma & -s_\alpha c_\gamma s_\beta - s_\gamma c_\alpha & c_\gamma c_\beta \end{bmatrix}, \tag{S27}$$

where $s_{(\cdot)}$ and $c_{(\cdot)}$ denote the sine and cosine of angle $(\cdot)$, respectively, and α, β, γ are rotation angles about the x_3, x_2, x_1 axes, respectively.

Recall that if vectors transform as $x'_i = R_{ij}x_j$, then second and fourth-order tensors transform as $\sigma'_{ij} = R_{ik}R_{j\ell}\sigma_{k\ell}$ and $C'_{ijk\ell} = R_{im}R_{jn}R_{ko}R_{\ell p}C_{mnop}$, respectively (similar expressions hold for transforming strain, ε_{ij}, and the compliance elasticity tensor, $Z_{ijk\ell} = C^{-1}_{ijk\ell}$). For convenience of computation, we convert to matrix notation by defining

$$\{\sigma\} = \begin{Bmatrix} \sigma_1 = \sigma_{11} \\ \sigma_2 = \sigma_{22} \\ \sigma_3 = \sigma_{33} \\ \sigma_4 = \sigma_{23} \\ \sigma_5 = \sigma_{13} \\ \sigma_6 = \sigma_{12} \end{Bmatrix}, \{\varepsilon\} = \begin{Bmatrix} \varepsilon_1 = \varepsilon_{11} \\ \varepsilon_2 = \varepsilon_{22} \\ \varepsilon_3 = \varepsilon_{33} \\ \varepsilon_4 = 2\varepsilon_{23} \\ \varepsilon_5 = 2\varepsilon_{13} \\ \varepsilon_6 = 2\varepsilon_{12} \end{Bmatrix}, \text{ and } \mathbf{D} = \begin{bmatrix} C_{1111} & C_{1122} & C_{1133} & C_{1123} & C_{1113} & C_{1112} \\ & C_{2222} & C_{2233} & C_{2223} & C_{2213} & C_{2212} \\ & & C_{3333} & C_{3323} & C_{3313} & C_{3312} \\ & & & C_{2323} & C_{2313} & C_{2312} \\ & \text{symm} & & & C_{1313} & C_{1312} \\ & & & & & C_{1212} \end{bmatrix}. \tag{S28}$$

From the stress and strain transformation laws in tensor notation, we can construct matrices, $\mathbf{M}$ and $\mathbf{N}$ that perform the transformations in matrix notation, where

$$\mathbf{M} = \left[\begin{array}{ccc|ccc} R_{11}^2 & R_{12}^2 & R_{13}^2 & 2R_{12}R_{13} & 2R_{13}R_{11} & 2R_{11}R_{12} \\ R_{21}^2 & R_{22}^2 & R_{23}^2 & 2R_{22}R_{23} & 2R_{23}R_{21} & 2R_{21}R_{22} \\ R_{31}^2 & R_{32}^2 & R_{33}^2 & 2R_{32}R_{33} & 2R_{33}R_{31} & 2R_{31}R_{32} \\ \hline R_{21}R_{31} & R_{22}R_{32} & R_{23}R_{33} & R_{22}R_{33}+R_{23}R_{32} & R_{21}R_{33}+R_{23}R_{31} & R_{22}R_{31}+R_{21}R_{32} \\ R_{31}R_{11} & R_{32}R_{12} & R_{33}R_{13} & R_{12}R_{33}+R_{13}R_{32} & R_{13}R_{31}+R_{11}R_{33} & R_{11}R_{32}+R_{12}R_{31} \\ R_{11}R_{21} & R_{12}R_{22} & R_{13}R_{23} & R_{12}R_{23}+R_{13}R_{22} & R_{13}R_{21}+R_{11}R_{23} & R_{11}R_{22}+R_{12}R_{21} \end{array}\right] \tag{S29}$$

and

$$\mathbf{N} = \left[\begin{array}{ccc|ccc} R_{11}^2 & R_{12}^2 & R_{13}^2 & R_{12}R_{13} & R_{13}R_{11} & R_{11}R_{12} \\ R_{21}^2 & R_{22}^2 & R_{23}^2 & R_{22}R_{23} & R_{23}R_{21} & R_{21}R_{22} \\ R_{31}^2 & R_{32}^2 & R_{33}^2 & R_{32}R_{33} & R_{33}R_{31} & R_{31}R_{32} \\ \hline 2R_{21}R_{31} & 2R_{22}R_{32} & 2R_{23}R_{33} & R_{22}R_{33}+R_{23}R_{32} & R_{21}R_{33}+R_{23}R_{31} & R_{22}R_{31}+R_{21}R_{32} \\ 2R_{31}R_{11} & 2R_{32}R_{12} & 2R_{33}R_{13} & R_{12}R_{33}+R_{13}R_{32} & R_{13}R_{31}+R_{11}R_{33} & R_{11}R_{32}+R_{12}R_{31} \\ 2R_{11}R_{21} & 2R_{12}R_{22} & 2R_{13}R_{23} & R_{12}R_{23}+R_{13}R_{22} & R_{13}R_{21}+R_{11}R_{23} & R_{11}R_{22}+R_{12}R_{21} \end{array}\right]. \tag{S30}$$

Then, substituting Hooke's Law, $\{\sigma\} = \mathbf{D}\{\varepsilon\}$, and the strain transformation law, $\{\varepsilon\} = \mathbf{N}^{-1}\{\varepsilon\}'$, into the stress transformation law, $\{\sigma\}' = \mathbf{M}\{\sigma\}$, we find that $\mathbf{D}' = \mathbf{MDN}^{-1} = \mathbf{MDM}^T = \mathbf{N}^T\mathbf{DN}$, where the last expression uses the fact that $\mathbf{R}^{-1} = \mathbf{R}^T$ since it is a product of proper orthogonal matrices [25].

Note that the elastic surface plots provided alongside the spinodal architectures in the main text (see Figures 2 and 3) provide a visual representation of the tensor transformation by showing the (homogenized) directional Young's modulus, normalized to the Young's modulus of the bulk material that the architecture is composed of. Consider the compliance elasticity matrix, $\mathbf{S} = \mathbf{D}^{-1}$, of a spinodal architected material. The Young's modulus along the x-direction of the reference (unprime) coordinate frame can be extracted as, $E_{11} = 1/S_{11}$. The Young's modulus in any other direction, E'_{11}, can be obtained in a similar way from $\mathbf{S}'$, where $\mathbf{S}' = \mathbf{D}'^{-1}$ is the compliance elasticity matrix in a rotated (prime) coordinate frame, obtained according to the tensor transformation laws described above. A value of E'_{11} can be obtained for any arbitrary rotation of the reference coordinate frame, according to rotation angles, α, β, and γ, about the x_3, x_2, x_1 axes, respectively. The elastic surface plots show the value of E'_{11} (as the radial coordinate) for each combination of rotation angles, α, β, and γ.

S4 Additional details of the design examples

In this section, algorithmic parameters and mesh information are provided for the three design examples provided in the main text. In addition, we provide the standard (solid) topology optimization solutions (i.e., considering a single, solid, isotropic candidate material) and their objective function values, f_0, used in the main text to evaluate the relative performance of the spinodal designs. Lastly, we include some additional discussion about the spinodal density distribution resulting from spinodal topology optimization.

S4.1 Topology optimization algorithmic parameters and computational resources

To control the magnitude of change in the design variables over the optimization iterations, we consider a move limit, $mv = 0.05$, for the spinodal selection and density design variables, $\mathbf{Z}$ and $\boldsymbol{\rho}$; and a move limit, $mv = 0.25$ radians, for the orientation design variables $\boldsymbol{\alpha}$, $\boldsymbol{\beta}$, and $\boldsymbol{\gamma}$. To avoid undesirable local optima we perform five continuation steps on the material interpolation parameters: $p = [1, 1.5, 2, 2.5, 3]$ and $\tilde{\gamma} = [0, 0.2, 0.5, 0.8, 1]$. Each continuation step is said to converge after reaching the maximum number of iterations, $\text{MaxIter} = [150, 100, 100, 50, 50]$, or the convergence tolerance, $\text{tol} = 0.02$ (where convergence is based on the change in the spinodal selection design variables from one iteration to the next). Once continuation on p and γ is completed, the ξ parameter that controls the sharpness of the Heaviside approximation (initially set to $\xi = 0.1$) is increased by 0.5 every 15 iterations until it reaches a maximum value of 25. The Heaviside threshold parameter, $\eta = 0.5$, throughout the whole optimization process. In each problem, the initial guess is specified such that the volume constraint is satisfied and each spinodal architected material has an equal volume (i.e., $z_{\ell i} = \overline{v}/\rho_\ell \ \forall \ell, i$ with $\rho_\ell = (\underline{\rho} + \overline{\rho})/2 \ \forall \ell$). At initialization, $\boldsymbol{\alpha} = \boldsymbol{\beta} = \boldsymbol{\gamma} = \mathbf{0}$.

For the cantilever problems, the filter exponent and radius are $q = 1$ and $R = 0.4$ cm, respectively, and the problem is solved on half of the domain (symmetry enforced at the centerline of the beam, parallel to the $x_1 - x_3$ plane) on a hex mesh with $324,000$ elements. For the GE bracket, the filter exponent and radius are $q = 1$ and $R = 0.4$ cm, respectively, and the problem is solved on a hex mesh with $464,280$ elements generated inside a triangulated surface (STL) obtained from a STEP file of GE's jet engine bracket [26]. For the craniofacial implant, the filter exponent and radius are $q = 1$ and $R = 0.3$ cm, respectively, and the problem is solved on a hex mesh with $395,720$ elements. To handle the low density regions we impose an Ersatz stiffness in the void elements equal to 10^{-4}. All problems were run using a Python 3.6.9 implementation on a machine with 24 Intel Xeon CPUs, 251 GB of RAM, and NVIDIA Titan Xp GPUs with 12 GB of RAM.

S4.2 Standard topology optimization solutions

Designs considering standard topology optimization with a single, solid, isotropic material are provided in **Figure S3** for each of the three design problems considered in the main text. These designs are based on the same algorithmic parameters and volume fraction limits considered for the spinodal problems reported in the main text (i.e., $\overline{v} = 0.05$ for the cantilever and the craniofacial implant; $\overline{v} = 0.075$ for the GE jet engine bracket).

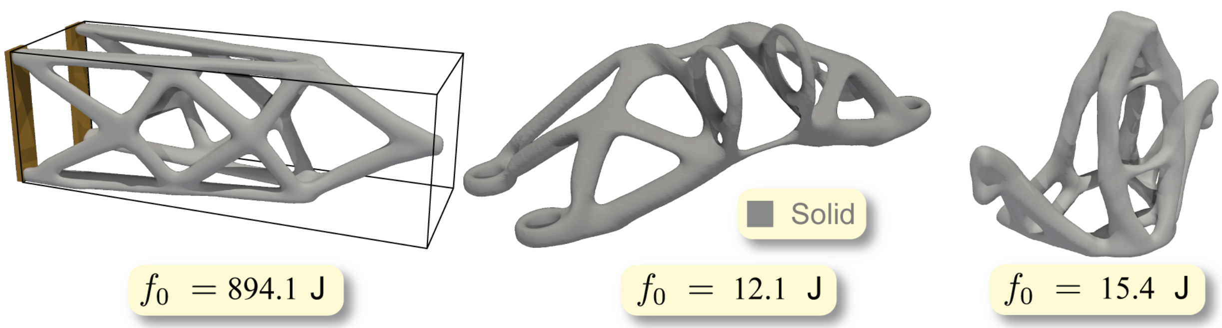

Figure S3: Standard topology optimization solutions considering a single, solid, isotropic material for the cantilever beam, GE jet engine bracket, and craniofacial implant.

S4.3 Spinodal density variation

The spinodal density variation is displayed in **Figure S4** for each of the three design problems with $0.3 \leq \rho \leq 0.7$ reported in the main text. Figure S4a provides the cut planes used in Figure S4b to show the spinodal density variation through the volume of each part. The spinodal density tends to be high in the interior of the structures and gradually decreases towards the boundaries. Similar spatially-varying spinodal density distribution in all optimized structures indicates that this type of arrangement maximizes the stiffness/weight ratio and highlights the value of providing freedom of spinodal density in the topology optimization framework. Furthermore, the histograms in Figure S4c clearly indicate that the upper and lower limits of spinodal density are prioritized. Note that the density filter and penalty on intermediate values of the design variables are imposed only on the spinodal selection design variables, $\mathbf{Z}$, but not on the spinodal density design variables, $\boldsymbol{\rho}$.

S5 Additive Manufacturing

All physical models were fabricated using the Original Prusa SL1 masked-stereolightography 3D printer (Prusa Research, Czech Republic), which shines UV light onto the underside of a resin vat, masked by a 2560×1440 pixel liquid crystal display (LCD) according to pixelated images (slices), to cure the part layer-by-layer. The pixel edge length is 47.25 μm and we print with a 50 μm layerheight. The build volume is $120.96 \times 68.04 \times 150$ mm. All models are built using Prusa's Grey Tough acrylate-based photopolymer resin with 8.5 second exposure time per layer. Slicing and spinodal-embedding are done with an in-house Matlab code described below and the generated black-and-white png images for each layer are provided to the 3D printer. No support was needed for the cantilever structures; thus, the slices from the Matlab code were sent directly to the 3D printer. For the GE bracket and craniofacial implant, the pixel data were converted to a surface representation (STL) file and imported into PrusaSlicer for support generation. These STL files were at the slicing software's file size upper limit; thus, a means to generate supports directly in the pixel representation will be desirable for larger-scale parts. Supports were only generated to support the macroscale features. Unsupported bridging features at the microscale had length scale well below the bridging capabilities of the m-SLA 3D printer.

S5.1 Processing optimized spinodal-embedded parts for additive manufacturing

The phase field representation of spinodal architected materials facilitates voxel-based communication of the spinodal-embedded topology optimized parts to a 3D printer. The build volume of the m-SLA 3D printer used here can be thought of as a 3D matrix of pixels (pixel grid). During printing, each pixel is filled with material or no material based on a binary pixelated image projected to the underside of the resin vat for each layer of the part. The coordinates of each pixel can be fed to the phase field function of each spinodal architected material to determine whether it should be assigned solid or void for that spinodal architected material.

The topology optimization fields, $\tilde{\mathbf{Y}}$, $\boldsymbol{\rho}$, $\boldsymbol{\alpha}$, $\boldsymbol{\beta}$, and $\boldsymbol{\gamma}$, defining the existance, porosity, and orientation of the spinodal architected materials, live on a coarser mesh than that of the spinodal features. To determine which spinodal architected material should exist in each pixel of the printer's build volume, $\tilde{\mathbf{Y}}$ is first projected to the printer's fine pixel grid and smoothed to remove artifacts of the coarse topology optimization mesh.

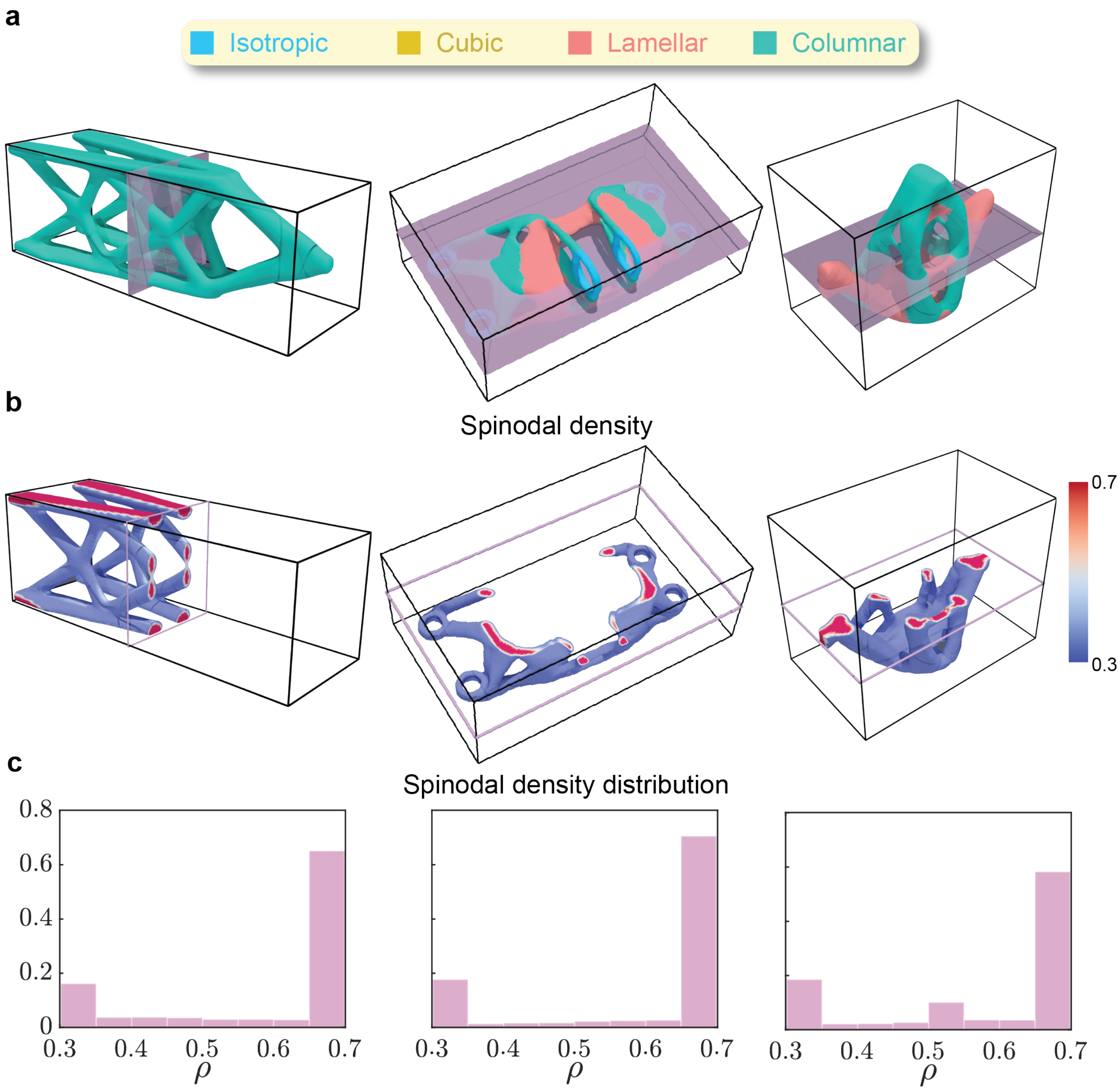

Figure S4: Spinodal density variation of the cantilever beam, GE jet engine bracket, and craniofacial implant considering spinodal density, $0.3 \leq \rho \leq 0.7$. **a** Spinodal architected material distribution and cut locations. **b** Spinodal density variation through cross-sections of the part. **c** Histograms of spinodal density distribution.

Note that due to the multi-material interpolation function, SIMP penalization, and Heaviside projection used during optimization, $\tilde{\mathbf{Y}}$ is close to binary; however, some intermediate values and mixing may remain. After projecting $\tilde{\mathbf{Y}}$ to the pixel grid, sets, $\mathcal{M}_i, i = 1, \ldots, m$, are defined to contain pixels in which spinodal architected material i dominates (i.e., pixel $\ell \in \mathcal{M}_i \iff \tilde{y}_{\ell i} = \max_{j=1..m} (\tilde{y}_{\ell j})$). Additionally, to avoid evaluating the spinodal phase fields for pixels that are outside of the macrostructure part, $\mathcal{P}$ is defined as the set of pixels falling within the macrostructure part boundary. Then, for each of the four spinodal architected material considered here, a discrete version of the spinodal phase field,

$$\phi^0_{\ell i}\left(\mathbf{x}_\ell\right) = \sqrt{\frac{2}{N}} \sum_{k=1}^{N} \cos\left(\kappa \left[\mathbf{R}\left(\tilde{\alpha}_\ell, \tilde{\beta}_\ell, \tilde{\gamma}_\ell\right) \mathbf{n}_{ki}\right] \cdot \mathbf{x}_\ell + \mu_k\right), \tag{S31}$$

is defined for $i = 1, \ldots, m$ and for all $\ell \in \mathcal{P} \cup \mathcal{M}_i$, where $\mathbf{x}_\ell$ is the centroidal coordinate of pixel ℓ. The set of $k = 1, \ldots, N$ wave vectors, $\mathbf{n}_{ki}$, precomputed for spinodal architected material i according to the appropriate θ_1, θ_2, θ_3 restrictions, is rotated according to the values of $\tilde{\alpha}_\ell$, $\tilde{\beta}_\ell$, and $\tilde{\gamma}_\ell$, which are projected to the fine pixel grid (without any smoothing) from the orientation design variables defined on the coarse topology optimization mesh. The spinodal feature size parameter, κ, controls the feature size of the printed spinodal architected materials and is chosen according to the printer's resolution and the size of the macrostructure.

The discrete phase field in Equation S31 defines a different spinodal architected material class and a different frame rotation for each pixel, which does not ensure that the spatially-varying spinodal architected material will be well-connected from one pixel to the next. Connectivity is enforced by interpolating the phase fields associated with each spinodal architected material according to (repeated from Equation 1 of the main text)

$$\phi_\ell\left(\mathbf{x}_\ell\right) = \frac{\sum_{i=1}^{m} \max\left[0, \left(1 - d_H\left(\mathbf{x}_\ell, \mathcal{M}_i\right)/R_\phi\right)\right]^{1/2} \phi^0_{\ell i}\left(\mathbf{x}_\ell, \tilde{\alpha}_\ell, \tilde{\beta}_\ell, \tilde{\gamma}_\ell\right)}{\sum_{i=1}^{m} \max\left[0, \left(1 - d_H\left(\mathbf{x}_\ell, \mathcal{M}_i\right)/R_\phi\right)\right]^{1/2}}, \tag{S32}$$

where d_H is the Hausdorff distance, R_ϕ is the radius of the interpolated phase field, and the $1/2$ exponent is a penalization. A graphical representation of Equation S32 is provided in Figure S5 to elucidate the spinodal phase field interpolation that leads to smooth transition between them. Then, a discrete version of the level set function (repeated from Equation 2 of the main text),

$$\chi_\ell\left(\mathbf{x}_\ell\right) = \begin{cases} 1 & \text{if } \phi_\ell\left(\mathbf{x}_\ell\right) \geq \phi_{\text{cut}}\left(\tilde{\rho}_\ell\right) \\ 0 & \text{otherwise,} \end{cases} \tag{S33}$$

is used to define the final solid-void assignment of each pixel, $\ell \in \mathcal{P}$, where $\tilde{\rho}_\ell$ is projected from the coarse topology optimization mesh to the fine pixel grid (without any smoothing). Finally, two-dimensional (2D),

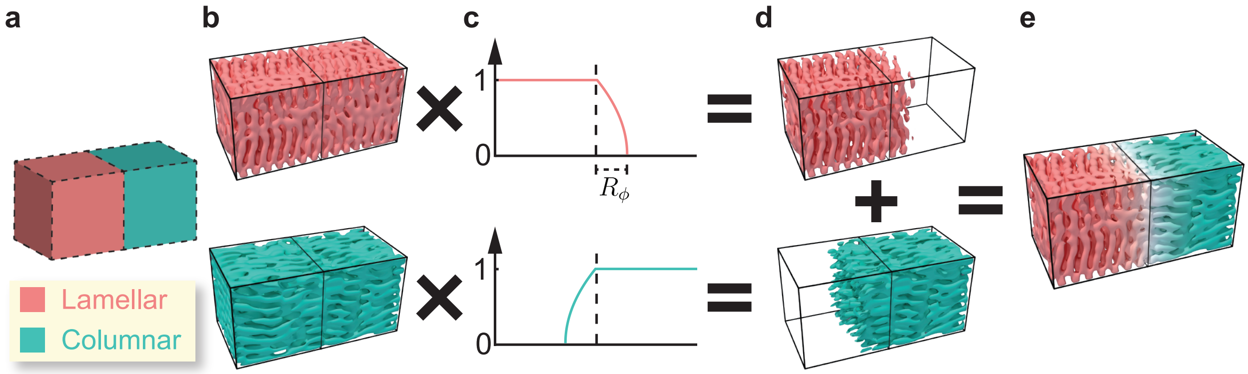

Figure S5: Graphical representation of the spinodal interpolation process described by Equation S32. **a** Two adjacent regions assigned lamellar and columnar spinodal architected materials with a discrete interface between them. **b** Lamellar and columnar spinodal microarchitectures generated via the phase fields represented by the term, $\phi^0_{\ell i}\left(\mathbf{x}_\ell, \tilde{\alpha}_\ell, \tilde{\beta}_\ell, \tilde{\gamma}_\ell\right)$, of Equation S32. **c** Interpolating term, $\max\left[0, \left(1 - d_H\left(\mathbf{x}_\ell, \mathcal{M}_i\right)/R_\phi\right)\right]^{1/2}$, of Equation S32. **d** Interpretation of the lamellar and columnar spinodal microarchitectures associated with the phase fields obtained by multiplying the previous two terms. **e** Final, spatially-varying spinodal microarchitecture obtained by adding the two resulting phase fields to achieve a smooth transition between the lamellar and columnar spinodal architected materials.

binary, pixelated images corresponding to each layer of the spinodal-embedded topology-optimized part are obtained directly from the discrete level set field and sent to the 3D printer. A flowchart of the entire process from optimization-based design to additive manufacturing is provided in the **Figure S6**.

The proposed voxel-based strategy will open opportunities in manufacturing spinodal-embedded structures using other materials, such as metals and composites, which have a broader range of properties (e.g., stiffness, heat conductivity) and applications (e.g., mechanical components, biomedical implants). The proposed approach is general and extendable, but will need to be tailored for each manufacturing platform. For example, with the m-SLA approach considered here, spinodal density limits were set based on limits on the bicontinuous nature of the solid and void phases and pore size limits were controlled by the printer resolution. In other systems, like laser powder bed fusion for metal parts, powder removal and desired geometric accuracy may require different limits on spinodal density and/or pore size. Additionally, the layer-wise pixel representation will need to be converted to a layer-wise scanpath. For only moderate scaling relative to the spinodal-embedded parts printed here, STL files become prohibitive and the toolpath will likely need to be generated directly from the pixel data.

S5.2 Spinodal parameters for manufacturing

To improve computational speed, the number of wave vectors is reduced to $N = 100$ when generating the physical phase field from the topology optimization results using Equation S31. The wavelength parameter, κ, used to control the length scale of the spinodal microarchitectures relative to the size of the macrostructure

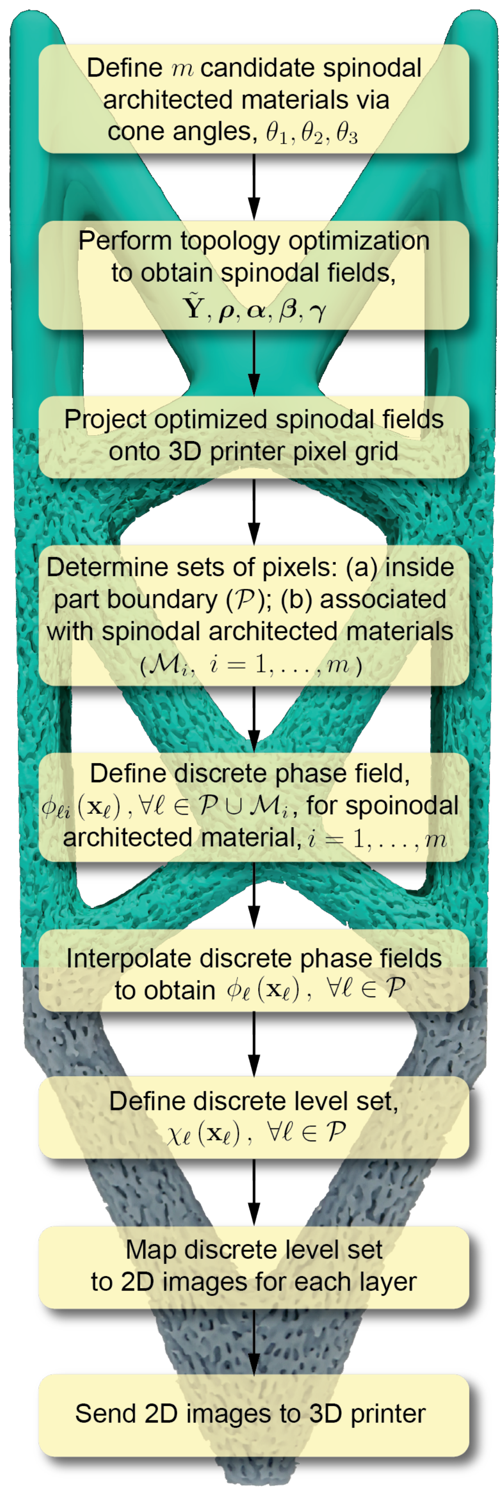

Figure S6: Flowchart of entire process from defining the design space and performing topology optimization to translating the data to a format the 3D printer can handle and manufacturing the part. The cantilever in the background shows the progression (from top to bottom) of the spinodal representation during design, after projection, and after manufacturing.

is different for each printed model. The cantilever beams are printed with largest dimension of the macroscale at 14.4 cm and $\kappa = 6$ cm^{-1}. The GE bracket and the craniofacial implant are printed with largest dimension of the macroscale at 17.9 cm and 8.1 cm, respectively, and $\kappa = 4$ cm^{-1}. The radius of the interpolated phase field in Equation S32 is $R_\phi = 0.2$ cm for all problems.

References

[1] K. Binder, *Reports on progress in physics* **1987**, *50*, 7 783.

[2] J. W. Cahn, J. E. Hilliard, *The Journal of chemical physics* **1958**, *28*, 2 258.

[3] C. M. Elliott, Z. Songmu, *Archive for Rational Mechanics and Analysis* **1986**, *96*, 4 339.

[4] J. W. Cahn, *The Journal of Chemical Physics* **1965**, *42*, 1 93.

[5] C. Soyarslan, S. Bargmann, M. Pradas, J. Weissmüller, *Acta Materialia* **2018**, *149* 326.

[6] S. Torquato, H. Haslach Jr, *Appl. Mech. Rev.* **2002**, *55*, 4 B62.

[7] S. Kumar, S. Tan, L. Zheng, D. M. Kochmann, *npj Computational Materials* **2020**, *6*, 1 1.

[8] G. Dong, Y. Tang, Y. F. Zhao, *Journal of Engineering Materials and Technology* **2019**, *141*, 1.

[9] A. Bensoussan, J.-L. Lions, G. Papanicolau, *Asymptotic analysis for periodic structures*, Elsevier, **1978**.

[10] M. P. Bendsøe, N. Kikuchi, *Computer Methods in Applied Mechanics and Engineering* **1988**, *71*, 2 197.

[11] E. D. Sanders, A. Pereira, G. H. Paulino, *Science Advances* **2021**, *7*, 16 eabf4838.

[12] B. Bourdin, *International Journal for Numerical Methods in Engineering* **2001**, *50*, 9 2143.

[13] T. Borrvall, J. Petersson, *Computer Methods in Applied Mechanics and Engineering* **2001**, *190* 4911.

[14] T. Zegard, G. H. Paulino, *Structural and Multidisciplinary Optimization* **2016**, *53*, 1 175.

[15] M. Zhou, G. Rozvany, *Computer Methods in Applied Mechanics and Engineering* **1991**, *89*, 1-3 309.

[16] M. P. Bendsøe, *Structural Optimization* **1989**, *1*, 4 193.

[17] J. K. Guest, J. H. Prévost, T. Belytschko, *International Journal for Numerical Methods in Engineering* **2004**, *61*, 2 238.

[18] F. Wang, B. S. Lazarov, O. Sigmund, *Structural and Multidisciplinary Optimization* **2011**, *43*, 6 767.

[19] X. S. Zhang, G. H. Paulino, A. S. Ramos Jr., *Structural and Multidisciplinary Optimization* **2018**, *57* 161.

[20] E. D. Sanders, M. A. Aguiló, G. H. Paulino, *Computer Methods in Applied Mechanics and Engineering* **2018**, 798–823.

[21] E. D. Sanders, A. Pereira, M. A. Aguiló, G. H. Paulino, *Structural and Multidisciplinary Optimization* **2018**, *58*, 6 2727.

[22] J. Stegmann, E. Lund, *International Journal for Numerical Methods in Engineering* **2005**, *62*, 14 2009.

[23] D. P. Bertsekas, *Nonlinear Programming*, Athena Scientific, 2 edition, **1999**.

[24] J. Nocedal, S. Wright, *Numerical optimization*, Springer Science & Business Media, **2006**.

[25] B. A. Auld, *Acoustic fields and waves in solids*, volume I, John Wiley & Sons, **1973**.

[26] G. Electric, GE jet engine bracket challenge, URL `https://grabcad.com/challenges/ge-jet-engine-bracket-challenge`, Accessed March 1, 2021.